A new dataset of rain cells generated from observations of the Tropical Rainfall Measuring Mission (TRMM) precipitation radar and visible and infrared scanner and microwave imager

Zhenhao Wu[1], Yunfei Fu[1], Peng Zhang[2], Songyan Gu[2], and Lin Chen[2]

[1]School of Earth and Space Sciences, University of Science and Technology of China, Hefei, 230026, China

[2]Key Laboratory of Radiometric Calibration and Validation for Environmental Satellites, National Satellite Meteorological Center, China Meteorological Administration, Beijing, 100081, China

Correspondence: Yunfei Fu (fyf@ustc.edu.cn)

Abstract. Rain cells are the most common units in the natural precipitation system. Enhancing the understanding of these rain cell characteristics can significantly improve the cognition of the precipitation system. Previous studies have mostly analyzed rain cells from a single radar data. In this study, we merged the precipitation parameters measured by the Tropical Rainfall Measuring Mission (TRMM) precipitation radar (PR) with the muti-channel cloud-top radiance measured by the visible and infrared scanner (VIRS) and the muti-channel brightness temperature measured by the TRMM microwave imager (TMI). The rain cells were identified within the PR orbit, and the swath truncation effect was eliminated. We used two methods for rain cell identification: the minimum bounding rectangle (MBR) method and the best fit ellipse (BFE) method, and compared the differences between these two methods in describing the rain cell characteristics. The results indicate that both methods can better reflect the geometric characteristics of rain cells. Compared with the MBR method, the BFE method can obtain a smaller rain cell area, and the filling ratio is better. However, the MBR method can simplify the data storage volume. Consequently, we employed the MBR method to analyze the precipitation structure of two typical rain cell precipitation cases. The results show that the new rain cell dataset can be used for the analysis of rain cell precipitation parameters and visible/infrared and microwave signals, which provides valuable data for comprehensive studies on the rain cell structural characteristics and furthers the understanding of precipitation mechanisms. The data which were used in this paper are freely available at https://doi.org/10.5281/zenodo.8352587 (Wu et al., 2023).

1 Introduction

31   Precipitation is an important part of the global energy and water cycle (Houze, 1997; Oki and Kanae,

32   2006; Lau and Wu, 2010). Rain cells are considered as the most basic precipitation unit, but they have

33   been defined differently in literatures. Austin and Houze (1972) studied the precipitation patterns in New

34   England and found that there are basically composed of subsynoptic scale precipitation regions, each

35   with rather clearly definable characteristics and behavior. Based on radar observations and detailed rain

36   gauge records, the precipitation patterns can be divided into synoptic areas, large mesoscale areas, small

37   mesoscale areas and cells. The rain cell with an area of about 10 km^2 radar echo is regarded as a single

38   cumulus convective unit in their study. Goldhirsh and Musiani (1986) defined rain cell as areas with rain

39   rates greater than or equal to the threshold by setting a corresponding rain rate threshold. Meanwhile,

40   many papers studied the relationship between precipitation rate threshold and rain cell size based on

41   ground-based radar data (Konrad, 1978; Sauvageot et al., 1999; Feral et al., 2000; Begum and Otung,

42   2009). Capsoni et al. (1987) defined rain cell as a connected region with a precipitation rate greater than

43   5 $mm\,h^{-1}$ based on S-band radar observation near Milan in 1980, and obtained the relationship between

44   the spatial number densities of rain cells and the cumulative distribution of precipitation rate. Awaka

45   (1989) modified the precipitation rate threshold to 0.4 $mm\,h^{-1}$.

46   In order to obtain the shape parameters, Feral et al. (2000) employed the elliptic fitting method to

47   investigate the geometric characteristics and directional distribution of rain cells. The statistical results

48   revealed that the major axis length was twice longer than the minor axis length for the majority of the

49   rain cells, and the direction distribution was uniform. When studying the horizontal dimensions of the

50   precipitation systems, Nesbitt et al. (2006) used the best-fit ellipse method to obtain the major axis and

51   minor axis. However, due to the limitation of the swath width, some precipitation systems were truncated.

52   The results indicated that there were obvious differences of storm morphology characteristics over land

53   and ocean, which may lead to significant differences in regional precipitation simulation. Liu and Zipser

54   (2013) investigated the different horizontal structures of convective precipitation systems in the tropics

55   and subtropics by using 14 years of Tropical Rainfall Measuring Mission (TRMM) Precipitation Radar

56   (PR) observations combined with the best ellipse fitting method. They found that line shaped convective

57   systems occurred more frequently over ocean, and showed higher frequency in the subtropics.

58   Fu et al. (2020) used the minimum bounding rectangle (MBR) method to identify rain cells and studied

59   the geometric and physical parameter characteristics of rain cells over tropical land and ocean areas with

60   15-yr measurements of the TRMM PR. The study showed that the average rain rate of rain cells is more

61 frequently related to the increase of area, and the increasing rate over land is greater than that over ocean.

62 Chen et al. (2021) used the same dataset in the above study to analyze the multidimensional

63 morphological characteristics of precipitation areas over the Tibetan Plateau in summer, and found that

64 there is a close relationship between the morphological characteristics of precipitation areas and the

65 intensity of precipitation.

66 The investigation of the three-dimensional structure of rain cells is helpful to understand the

67 thermodynamic structure and microphysical processes within precipitation systems (Houze, 1981; Zipser

68 and Lutz, 1994; Yuter and Houze, 1995; Liu and Fu, 2001). The PR onboard the TRMM provides an

69 excellent opportunity to study the 3D structure of precipitation (Kummerow et al., 1998, 2000; Nesbitt

70 et al., 1999; Schumacher and Houze, 2003; Li and Fu, 2005), and the visible and infrared scanner (VIRS)

71 on the satellite can provide spectral signals and cloud parameters information on the top of precipitation

72 clouds (Liu and Fu, 2010; Fu, 2014), the TRMM microwave imager (TMI) can provide information of

73 different phase particles inside precipitation clouds (Viltard et al., 2000; He et al., 2006; Fu et al., 2021).

74 Fu et al. (2007a) analyzed the characteristics of precipitating and non-precipitating clouds in typhoon

75 Ranan occurred in August 2004 by matching and merging data measured by TRMM PR, TMI and VIRS.

76 The result indicated that large particles are mostly in the precipitation cloud, and the effective radius

77 distribution of non-precipitating cloud particles is relatively wide. Fu et al (2007b) utilized the results of

78 multi-instrument measurements on TRMM to analyze several typical precipitation systems over the East

79 Asia, and reveal the relationship of precipitation structure, lightning activities, precipitation cloud top

80 and rainfall rate near surface. Liu et al (2008) established a precipitation feature database based on 9

81 years of TRMM observation data, matching the VIRS and TMI observation results to PR pixels resolution.

82 Subsequently, Liu et al (2009) used this database to study the contribution of warm rain systems to

83 precipitation over the tropics and obtained the seasonal and spatial distribution of warm rain systems.

84 This paper is merging the PR, VIRS, and TMI measurements at PR pixel resolution, and combining

85 the rain cell identification method to establish a new precipitation parameter and visible/infrared and

86 microwave signal dataset. Section 2 describes the data and merging methods. Section 3 introduces the

87 definition method of rain cells and identification method. Section 4 defines the geometric and physical

88 parameters of rain cells. In Section 5, the statistical results of rain cell parameters are given and the

89 structures of two typical rain cells are analyzed. Access to the datasets is introduced in Sect. 6, and

90 conclusions are presented in Sect. 7.

2 Data

2.1 Tropical Rainfall Measuring Mission

The TRMM was jointly developed by the US National Aeronautics and Space Administration (NASA) and the Japan Aerospace Exploration Agency (JAXA) and launched on November 27, 1997. The TRMM is a non-solar synchronous polar-orbiting satellite with an orbital inclination of 35° and observes a location between 38°S and 38°N (Simpson et al., 1996; Kummerow et al., 1998,2000). The satellite carries five instruments: PR, VIRS, TMI, the Lighting Imaging Sensor (LIS), the Cloud and Earth Radiant Energy Sensor (CERES). This study mainly involves the measurements of TRMM PR, VIRS, and TMI.

2.2 PR and 2A25 dataset

The PR was the first spaceborne precipitation radar onboard the TRMM. It is a single-frequency microwave radar with a frequency of 13.8 GHz (Kummerow et al., 1998; Kozu et al., 2001). PR scans in the cross-track direction with a scanning inclination of 17°. There are 49 pixels on each scanning line. The horizontal resolution is about 4.3 km at nadir (5.0 km after the orbital boost), and the scanning width is 215 km (245 km after the orbital boost). It can detect the three-dimensional structure of precipitation from mean sea level to 20 km (a total of 80 layers) with a vertical resolution of 0.25 km.

The 2A25 data is the second-level data product of the TRMM PR, which is generated by inverting the echo signals detected by the PR. This dataset mainly includes scanning time, geographic information, three-dimensional rain rate, rain type and so on (Awaka et al., 1997). The detection sensitivity of the PR is about 17 dBZ, corresponding to the rain rate of about 0.4 $mm\,h^{-1}$ (Schumacher and Houze, 2003). Therefore, when the rain rate of the pixels is lower than 0.4 $mm\,h^{-1}$, the default value is set and will not be involved in the calculation.

2.3 VIRS and 1B01 dataset

The VIRS scans in the cross-track direction with a scanning angle of 45°. There are 261 pixels on each scanning line. The scanning width is 720 km (833 km after the orbital boost), and the horizontal resolution is 2.2 km at nadir (2.4 km after the orbital boost). It has five channels from visible to the far infrared band: CH1 (0.63 μm), CH2 (1.6 μm), CH3 (3.7 μm), CH4 (10.8 μm) and CH5 (12.0 μm).

The 1B01 is a first-level data product of VIRS, which includes the reflectivity (RF1, RF2) and the infrared radiation brightness temperature ($TB_{3.7}$, $TB_{10.8}$, $TB_{12.0}$) after the correction and calibration of

4

122   the VIRS detection results.

123

2.4 TMI and 1B11 dataset

125   The TMI is a nine-channel passive microwave radiometer with five frequencies spanning from 10 to 85

126   GHz. The microwave signal frequencies are 10.65, 19.35, 21.3, 37.0, and 85.5 GHz, except for 21.3 GHz,

127   which is a single vertical polarization channel. The other four frequencies are horizontal (H) and vertical

128   (V) polarization dual channels. The scanning width is 760 km (878 km after the orbital boost). The

129   horizontal resolution of each frequency channel (effective field of view of beam, Kummerow et al., 1998)

130   varies from 63 km × 37 km at 10.65 GHz to 7 km × 5 km at 85.5 GHz. The 1B11 data contains the

131   calibrated TMI-detected microwave brightness temperature at multiple channels.

132

2.5 2A25, 1B01 and 1B11 merged data

134   To comprehensively analyze the parameters of precipitation, cloud top spectral signal and particle phase

135   in the cloud precipitation system, the 2A25, 1B01 and 1B11 data products (derived from the TRMM PR,

136   VIRS and TMI, respectively) were matched and merged. Due to the difference in data detection methods,

137   the spatial resolution is different for the three instruments, but the time lag between detections of the

138   same target is less than 1 min. It provides the possibility of data merging because of the quasi-

139   synchronous detection. In this paper, we default to the consistency of time during data merging, only

140   considering spatial merging. Based on the pixel resolution of PR detection, VIRS and TMI are matched

141   to corresponding pixels according to latitude and longitude (Liu et al., 2008; Fu et al., 2011; Sun and Fu,

142   2021).

143   For the PR and VIRS, in order to obtain the spectral signals (reflectivity and infrared radiation

144   brightness temperature) near the precipitation cloud top, the horizontal resolution of 1B01 pixel is

145   decreased to make it consistent with 2A25. Generally, there are usually about 7 VIRS pixels near 1 PR

146   pixel. The specific method is to introduce the Gaussian function. The spectral signals are calculated by

147   weighted averaging the VIRS near the PR pixel. It was found that the spectral signals changed weakly

148   after merging, the mean change was less than 0.7%, and the mean square deviation was less than 2.5%

149   (Fu et al., 2011). Sun and Fu (2021) considered the merging process between the PR and VIRS pixels

150   was no dramatic variations on the original data, and the conclusions were consistent with Fu et al. (2011).

151   For TMI, the measured values in different bands have different spatial resolutions. In order to obtain

152   the microwave radiation brightness temperature in PR pixel resolution, it is necessary to increase the

153 horizontal resolution of 1B11 pixels to make it consistent with the resolution of 2A25 pixels. By using

154 the nearest neighbor method, each PR pixel is assigned a TMI pixel closest to it (Liu et al., 2008).

3 Algorithm of rain cell identification

156 Previous studies have pointed out that the measurements of PR are inevitably affected by the swath

157 truncation effect due to the limitation of the PR detection orbit. Nesbitt et al. (2006) analyzed 3-year

158 TRMM PR data and concluded that nearly 42% of total rainfall is affected by the swath truncation. Liu

159 and Zipser (2013) showed that due to the influence of swath truncation, the parameters described rain

160 cell would be distorted and the captured precipitation systems would be incomplete. Fu et al. (2020)

161 defined rain cell as neighboring rain pixels with at least 0.4 $mm\ h^{-1}$ near-surface rain rate or 17 dBZ

162 reflectivity by using the PR data. The rain cells affected by the swath truncation were removed in the

163 study, and the rain cells completely detected by PR swath were retained.

164 This paper also adopts the same definition and elimination method of rain cells proposed by Fu et al.

165 (2020). Firstly, using the eight-connected region method identifies the continuous region of rain pixels.

166 For example, for any rain pixel A, iteratively search its neighboring pixels (a total of 8 pixels). If one or

167 more of them are also rain pixels (marked as B, C, ⋯), A, B, C and ⋯ are identified as the same rain

168 cell. Then, the search process is repeated for B, C, ⋯ rain pixels until all adjacent pixels of any rain

169 pixel in the rain cell are non-precipitation pixels. Upon completion of the identification process for a rain

170 cell, the identified rain cell is numbered. Secondly, the rain pixel swath truncation identification and the

171 elimination of micro-rain cells (less than 4 pixels) are executed. The identified rain cells are

172 systematically traversed. When a rain cell edge is identified as located at the edge of the track, it is

173 defined as a truncated rain cell. If the number of pixels in a rain cell is less than 4, it is defined as a micro

174 rain cell. The above rain cells will be removed (Chen, 2019).

175 To describe the shape of the rain cell, the minimum bounding rectangle (MBR) rain cell identification

176 method and the best fit ellipse (BFE) rain cell identification method are used to identify the rain cell. The

177 MBR rain cell identification method is to find the rectangle with the smallest area covering the target

178 object (rain cell) by rotating the external rectangle (Fu et al., 2020). The BEF rain cell identification

179 method fits the most suitable elliptical shape wrapped rain cell according to the polygonal connection

180 frame of the outer boundary of the rain cell (Nesbitt et al., 2006).

4 Definitions of parameters of rain cell

182   We define some geometric and physical parameters to describe the identified rain cells (Fu et al., 2020).

183   The specific geometric parameters are listed in Table 1, where the first six parameters are called the

184   horizontal geometric parameters and the rest are the vertical geometric parameters. The differences in

185   geometric parameters of the MBR method and the BFE method are studied. Where α represents the

186   horizontal shape of the rain cell, a small (large) α indicates that the two-dimensional shape of the rain

187   cell is more like a strip (square) system, and has more (less) correlation with a frontal system. The

188   variable β expresses the ratio of the rain cell area (S_{rain}) to the area of the identification frame (S), and

189   characterizes the internal organization within the rain cell. Large (small) β suggests that those rain

190   pixels are more (less) compactly organized, and are more (less) likely to be associated with strong

191   convective systems. The variables γ_{max} and γ_{av} represent the three-dimensional spatial shape of the

192   rain cell. Small γ_{max} (γ_{av}) indicates a "squatty" appearance of rain cell, in contrast to a "lanky"

193   appearance for large γ_{max} (γ_{av}).

194

195   **Table 1. Definitions of geometric parameters of rain cell.**

Symbol	Geometric meaning of rectangle	Geometric meaning of ellipse
L (km)	r_L (km)	e_L (km)
	Length of the MBR method	Length of the major axis of the BFE method
W (km)	r_W (km)	e_W (km)
	Width of the MBR method	Width of the minor axis of the BFE method
α	r_α	e_α
	Horizontal shape of rain cell, $r_\alpha = r_W/r_L$	Horizontal shape of rain cell, $e_\alpha = e_W/e_L$
S_{rain} (km^2)	Area of the rain cell, sum of all areas of rain pixels	
S (km^2)	r_S (km^2)	e_S (km^2)
	Area of the MBR method, $r_S = r_L * r_W$	Area of the BFE method, $e_S = \frac{\pi}{4} * e_L * e_W$
β	r_β	e_β
	Filling ratio of the rain cell, $r_\beta = S_{rain}/r_S$	Filling ratio of the rain cell, $e_\beta = S_{rain}/e_S$
H_{max} (km)	Maximum echo top height among rain pixels in the rain cell	
H_{av} (km)	Mean echo top height averaged among rain pixels in the rain cell	
γ_{max}	Maximum spatial morphology, $\gamma_{max} = H_{max}/L$	
γ_{av}	Mean spatial morphology, $\gamma_{av} = 2H_{av}/(L + W)$	
H_{avc} (km)	Mean echo top height of convective precipitation in the rain cell	
H_{avs} (km)	Mean echo top height of stratiform precipitation in the rain cell	

196

197   Since the rain cell dataset contains the measurements of multiple instruments, we define some physical

198   parameters (Table 2) based on rain type, rain rate profiles, near surface rain rates, visible reflectivity and

199   infrared brightness temperature. Those parameters are significant to represent the intensity, the

200   inhomogeneity, and the evolution stage of rain cells.

201

202   **Table 2. Definitions of physical parameters of rain cell.**

| Symbol	Physical meaning
RR_{ave} (mm h^{-1})	Mean rain rate obtained by averaging all rain rates within the rain cell
RR_{max} (mm h^{-1})	Maximum rain rate among rain pixels of the rain cell
RR_{avc} (mm h^{-1})	Mean convective rain rate averaged by all convective rain rates within rain cell
RR_{avs} (mm h^{-1})	Mean stratiform rain rate averaged by all stratiform rain rate within rain cell
RR_{maxc} (mm h^{-1})	Maximum rain rate among convective pixels of the rain cell
RR_{maxs} (mm h^{-1})	Maximum rain rate among stratiform pixels of the rain cell
CAF (%)	Fraction of convective area to total precipitation area within the rain cell
SAF (%)	Fraction of stratiform area to total precipitation area within the rain cell
CPC (%)	Convective precipitation contribution to total precipitation within the rain cell
SPC (%)	Stratiform precipitation contribution to total precipitation within the rain cell
dBZ_{max} (dBZ)	Maximum radar reflectivity factor among rain pixels of the rain cell
H_dBZ_{max} (km)	Height of the maximum radar reflectivity factor among rain pixels of the rain cell
RF_{ave}	Mean reflectivity obtained by averaging all reflectivities of channel within the rain cell
RF_{avc}	Mean convective reflectivity averaged by all convective reflectivities of channel within the rain cell
RF_{avs}	Mean stratiform reflectivity averaged by all stratiform reflectivities of channel within the rain cell
TB_{ave} (K)	Mean brightness temperature obtained by averaging all brightness temperatures of channel within the rain cell
TB_{avc} (K)	Mean brightness temperature averaged by all convective brightness temperatures of channel within the rain cell
TB_{avs} (K)	Mean brightness temperature averaged by all stratiform brightness temperatures of channel within the rain cell

203

5 Results

5.1 Statistics of rain cell parameters

206   In this study, we select two methods for identifying rain cells. It is important to note that the choice of
207   identification method may influence the results of parameters. Taking the two rain cells shown in Figure
208   1 as example, they locate on the southern slope of the Tibetan Plateau (orbit 08691 on 2 June, 1999) and
209   the eastern part of the Tibetan Plateau (orbit 31787 on 13 June, 2003), respectively. Table 3 shows the
210   calculated horizontal geometric parameters of the rain cells displayed in Fig. 1.

211   The first case shown in Fig. 1a is calculated by the MBR method with r_L = 290.86 km, r_W = 140.29

212   km, S_{rain} = 10223.5 km², r_S = 40803.36 km², and r_β = 0.25, which shows a strip shape (r_α = 0.48).

213   For the second case (Fig. 1b), r_L, r_W, S_{rain}, r_S, and r_α are 169.57 km, 76.18 km, 4496.4 km²,

214   12917.48 km², and 0.45, respectively. In addition, the filling ratio in the second case (0.35) is slightly

215   larger than that in the first case (0.25), resulting in a more compact rain cell system overall.

216

217
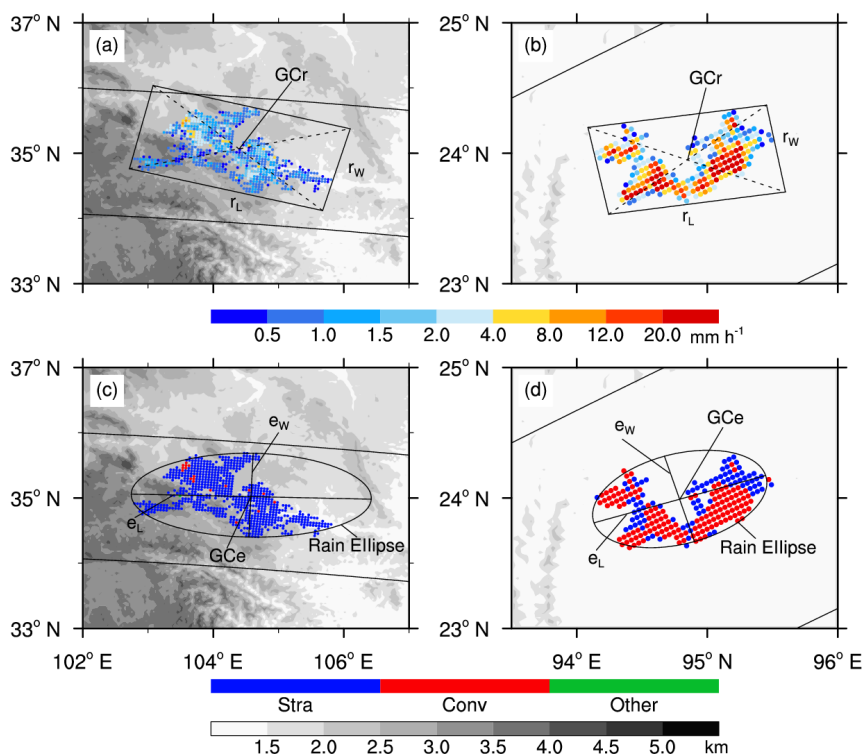
Figure 1. Near surface rain rate of two rain cells that occurred on 2 June 1999 (a) and on 13 June 2003 (b)
measured by PR. In (c, d), rain pixels with blue, red, and green represent stratiform, convective, and other
precipitation, respectively. The identification boxes are captured by the MBR method (a, b) and the BFE
method (c, d) for two rain cells.

222

223   The first case (Fig. 1c) is calculated by the BFE method with e_L = 347.63 km, e_W = 139.94 km, e_S

224   = 38207.27 km², e_α = 0.4, and e_β = 0.27. For the second case (Fig. 1d), e_L, e_W, e_S, e_α, and e_β are

225   170.66 km, 76.76 km, 10289.43 km², 0.45, and 0.44, respectively. Based on the horizontal geometric

226   parameters of rain cells captured by the MBR and BFE method, it is evident that the area of the

227   rectangular box is larger than that of the ellipse box. This difference in area results in a smaller filling

228   ratio for the MBR method as compared to the BFE method. There is no significant difference between

229   the two methods in terms of other geometric parameters. In practical application, compared with the BFE

230   method, the MBR method can greatly simplify the amount of data storage. Moreover, the MBR method

231   can envelop all the pixels of the rain system, which works better than the BFE method in bow

232   precipitation and small precipitation system (Chen, 2019).

233

234   **Table 3. The horizontal geometric parameters of the first/second case calculated by MBR and BFE.**

Rectangle		Ellipse	
$r_L(km)$	290.86/169.57	$e_L(km)$	347.63/170.66
$r_W(km)$	140.29/76.18	$e_W(km)$	139.94/76.76
r_α	0.48/0.45	e_α	0.4/0.45
$S_{rain}(km^2)$	10223.50/4496.40	$S_{rain}(km^2)$	10223.50/4496.40
$r_S(km^2)$	40803.36/12917.48	$e_S(km^2)$	38207.27/10289.43
r_β	0.25/0.35	e_β	0.27/0.44

235

236   The results of the parameter calculations shown in Table 4 are not affected by the rain cell identification

237   method. For the first case, the H_{max} = 8.75 km, H_{av} = 5.59 km, γ_{max} = 0.03, and γ_{av} = 0.026 show

238   that the vertical scale of the rain cell is at least one order of magnitude smaller than the horizontal scale.

239   The rain cell has RR_{ave} = 1.27 and RR_{max} = 8.08 mm h^{-1}, respectively. The parameters of CAF =

240   2.6 %, SAF = 97.3 %, CPC = 11% and SPC = 89% indicate that the rain cell is primarily composed of

241   stratiform precipitation. The maximum radar reflectivity factor (dBZ_{max}) is 36.38 dBZ, and the relative

242   height (H_dBZ_{max}) is 3.25 km. According to the merged data of VIRS and TMI instruments, the $RF1_{ave}$,

243    $TB_{10.8\_ave}$, $TB_{19GHz\_H\_ave}$, $TB_{85GHz\_H\_ave}$ are 0.72, 253.65 K, 260.61 K, and 254.44 K, respectively.

244   These parameters indicate that the stratiform rain cell has less precipitation and weak development.

245

246   **Table 4. The vertical geometric and physical parameters of the first/second case.**

Vertical parameter		Physical parameter			
$H_{max}(km)$	8.75/17.75	RR_{ave} (mm h^{-1})	1.27/11.64	$RF1_{ave}$	0.72/0.69
H_{av} (km)	5.59/9.47	RR_{max} (mm h^{-1})	8.08/113.14	$RF1_{avc}$	0.73/0.66
γ_{max}	0.03/0.11	RR_{avc} (mm h^{-1})	5.52/17.35	$RF1_{avs}$	0.72/0.73
γ_{av}	0.03/0.08	RR_{avs} (mm h^{-1})	1.16/2.31	$TB_{10.8\_ave}$ (K)	253.65/222.96
H_{avc} (km)	5.76/10.39	RR_{maxc} (mm h^{-1})	8.08/113.14	$TB_{10.8\_avc}$ (K)	252.42/221.51
H_{avs} (km)	5.58/7.96	RR_{maxs} (mm h^{-1})	4.45/11.87	$TB_{10.8\_avs}$ (K)	253.68/225.31
		CAF (%)	0.03/0.62	$TB_{19GHz\_H\_ave}$ (K)	260.61/276.75
		SAF (%)	0.97/0.38	$TB_{19GHz\_H\_avc}$ (K)	258.38/275.79
		CPC (%)	0.11/0.92	$TB_{19GHz\_H\_avs}$ (K)	260.66/278.32

Earth System
Science
Data
Open Access   Discussions

SPC (%)	0.89/0.08	$TB_{85GHz\_H\_ave}$ (K)	254.44/219.11
dBZ_{max} (dBZ)	36.38/57.81	$TB_{85GHz\_H\_avc}$ (K)	252.84/212.72
H_dBZ_{max} (km)	3.25/2.75	$TB_{85GHz\_H\_avs}$ (K)	254.49/229.53

247

248   For the second case, the H_{max} and H_{av} are 17.75 km and 9.47 km. The parameters γ_{max} = 0.11 and

249   γ_{av} = 0.08 are slightly larger than those in the first case, indicating that the second rain cell is slightly

250   taller than the first one. The parameters RR_{ave} and RR_{max} are 11.64 and 113.14 mm h^{-1} at this rain

251   cell, respectively, which are much larger than those in the first case. In addition, CPC (SPC) in the second

252   case has a value of 92% (8%), larger (smaller) than that in the first case. This indicates that the rain cell

253   in the first case has a greater proportion of stratiform precipitation in the total precipitation (89%), while

254   the second rain cell has a higher proportion of convective precipitation (92%). The parameters dBZ_{max}

255   and H_dBZ_{max} are 57.81 dBZ and 2.75 km, respectively. Compared with the first case, this case has

256   more precipitation and strong convective regions locate in lower layers. Furthermore, $RF1_{ave}$ has a

257   value of 0.69, slightly larger than that in the first case. Except for $TB_{19GHz\_H\_ave}$ = 276.75 K, the

258    $TB_{10.8\_ave}$ = 222.96 K and $TB_{85GHz\_H\_ave}$ = 219.11 K are smaller than the first case. This indicates that

259   the brightness temperature near the cloud top of the rain cell is relatively low, while the convection

260   develops vigorously and there is a higher concentration of ice particles within the cloud.

261

262   ## 5.2 Structure of rain cell

263

264   In order to further understand the rain cells, the structural distribution of rain cells is given in this section.

265   We also compare the distribution of relevant parameters between the original datasets and the merged

266   datasets. Figure 2 presents the signals detected by the visible, and thermal infrared channels of VIRS

267   onboard TRMM. The solid black line represents the TRMM PR scan track, while the solid red line is the

268   rectangular box of the rain cell. The reflectivity at 0.63 μm is primarily related to cloud optical thickness

269   (COT), and the higher the COT value, the greater the reflectivity. The equivalent brightness temperature

270   of a blackbody at 10.8 μm indicates the height of cloud top, and the higher the cloud top, the lower the

271   brightness temperature of the infrared channel (Luo et al., 2020).

272
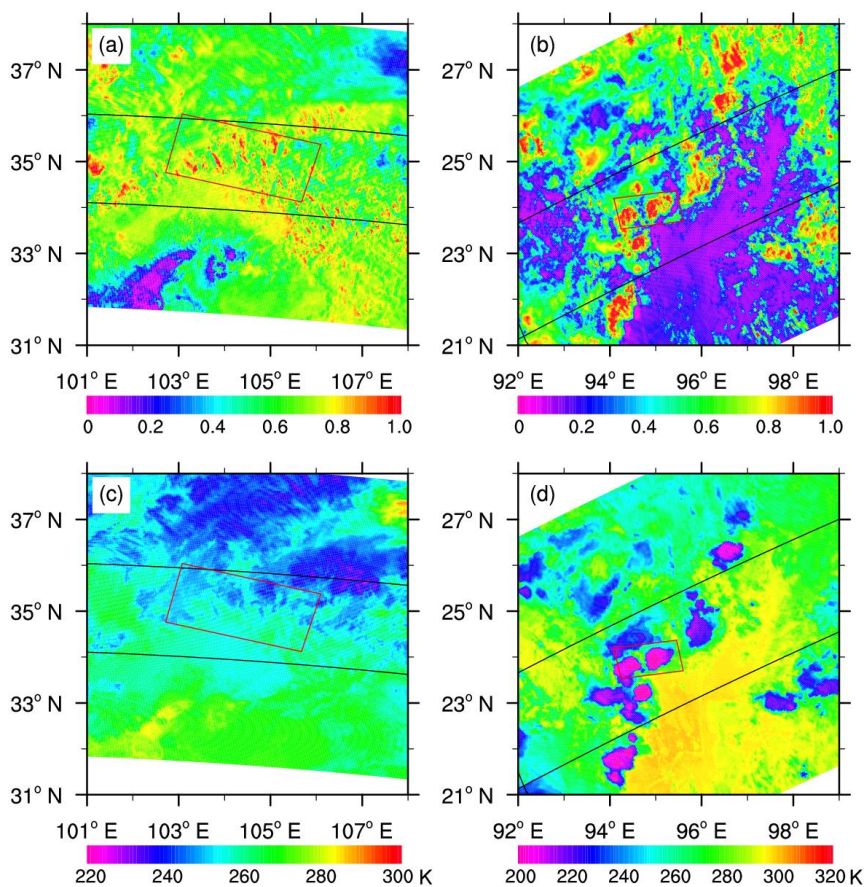
Figure 2. The distribution of (a, b) RF1 and (c, d) TB$_{10.8}$ for two precipitation cases. The solid black line is the TRMM PR scanning track and the solid red line is the rectangular box of rain cell.

In Fig. 2a, the reflectance of the visible channel in the rectangular box generally exceeds 0.6, with certain areas exhibiting values above 0.8. This suggests that the COT of certain areas of the stratiform rain cell is large. In addition, the brightness temperature of the 10.8 μm is mainly between 240-260 K (Fig. 2c), with low cloud development. There are two central regions with RF1 higher than 0.8 and corresponding TB$_{10.8}$ below 220 K (Figs. 2b, d). This suggests that there are many large-sized and deep ice cloud droplets dominating in the central region of the convective rain cell, with high cloud development. This analysis indicates that the signals obtained by TRMM/VIRS has strong detection ability for the cloud-top structure, and can have a good understanding of the development of the rain cell.

According to the theory of microwave remote sensing, the frequency of 10-23 GHz is sensitive to liquid water particles in the cloud, and the frequency of 36-89 GHz is sensitive to liquid and solid

Earth System
Open Access
Science
Discussions
Data

287   particles (ice or snow) in the cloud (Petty, 1994a, 1994b; Fu et al., 2021). Figure 3 shows the brightness

288   temperature distribution of the 19 GHz and 85 GHz horizontal polarization channels observed by the

289   TMI. The outline of rain cells cannot be clearly observed for the two cases in Figs. 3a, b, because the

290   emission signal of precipitation particles in the cloud is drowned by the surface emission signal, which

291   is why passive microwave low-frequency signals cannot invert the land surface precipitation (Fu et al.,

292   2021). Figure 3c shows TB_{85GHz_H}, which ranges between 240 and 260 K. The outline of the rain cell

293   can be roughly observed. The TB_{85GHz_H} of two convective central zones in rain cell are around 200-

294   220 K (Fig. 3d), indicating that ice-phase particles are more abundant in the convective precipitation

295   clouds.

296
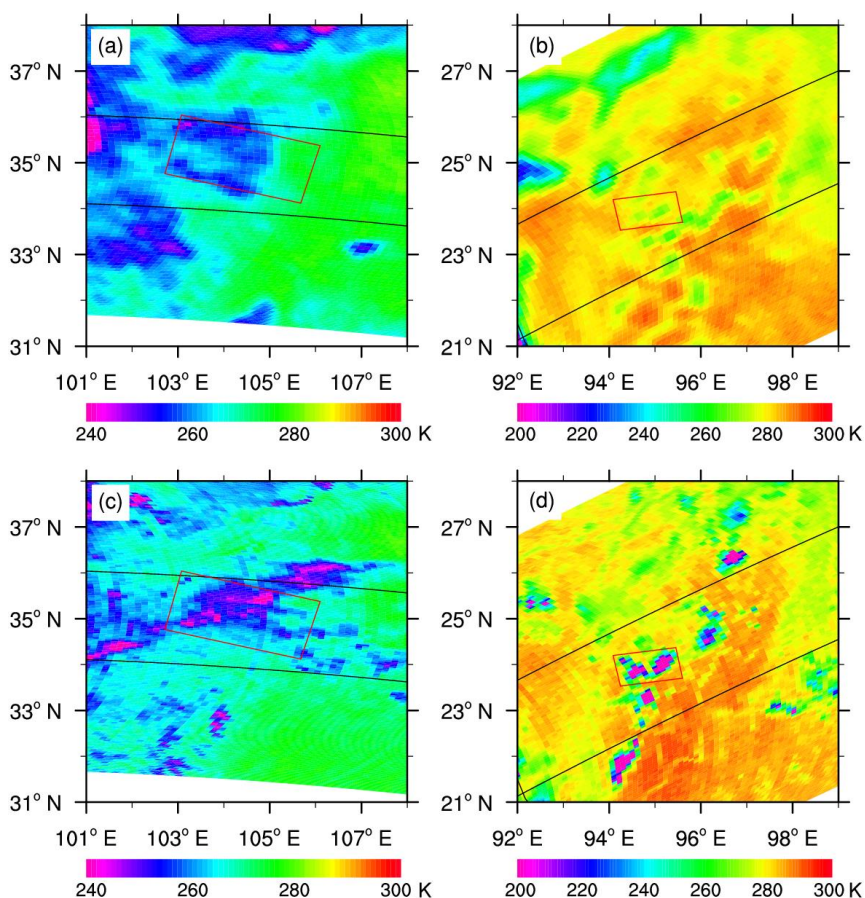
Figure 3. The same as Fig. 2, but for the (a, b) TB_{19GHz_H} and (c, d) TB_{85GHz_H}.

299

300   Figure 4 shows the distribution of parameters in the rain cells merged dataset. The stratiform rain cell

301 shown in the first case (Fig. 4a) has a uniform distribution of precipitation, with the maximum rain rate

302 exceeding 4 mm h^{-1}. However, the convective rain cell in the second case (Fig. 4b) presents a non-

303 uniform distribution, with large local variations, and the maximum rain rate can reach more than 20

304 mm h^{-1}. RF1 in the first case ranges between 0.6 and 0.8 (Fig. 4c). The value in the second case can

305 exceed 0.8 in the area of heavy precipitation, and the corresponding COT is larger (Fig. 4d). $TB_{10.8}$

306 varies from 240 to 260 K in the first case, and the cloud top height of rain cell is uniformly distributed

307 (Fig. 4e). While the $TB_{10.8}$ in the center of heavy precipitation varies between 200-220 K, which

308 suggests that the cloud top of the center region develops at a high altitude, whereas the altitude of the

309 cloud system around it is relatively low (Fig. 4f). TB_{19GHz_H} for two cases cannot observe valid

310 information due to the surface emissivity. The TB_{85GHz_H} varies uniformly from 240-260 K, which is

311 close to the distribution of the $TB_{10.8}$ (Fig. 4i). The region in the center of the strong precipitation in

312 Fig. 4j is below 200 K, which indicates that the cloud interior contains more ice-phase particles. In a

313 word, the merging process has no dramatic variations on the distribution of original data.

314
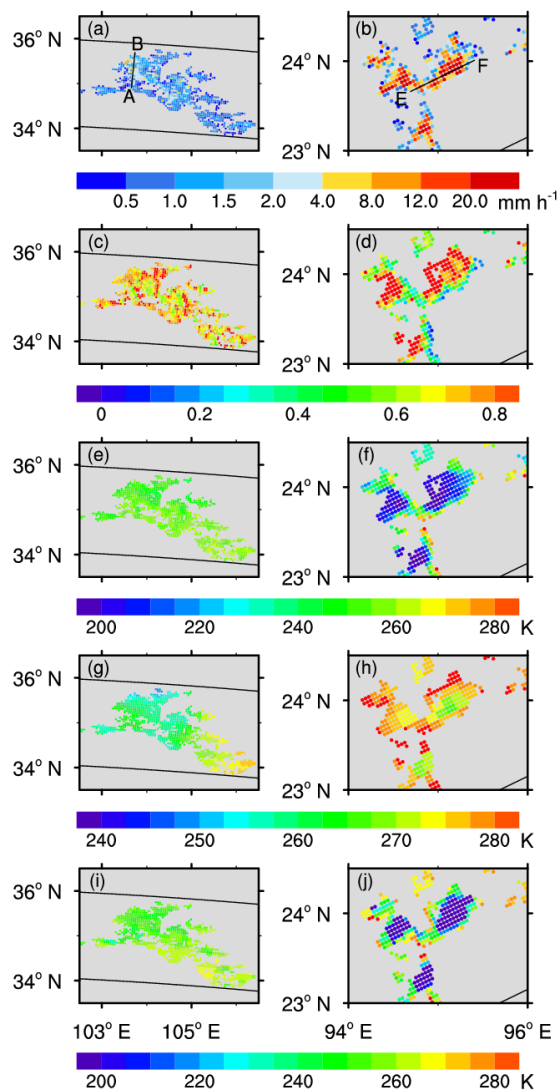
Figure 4. The distributions of (a, b) the near-surface rain rate, (c, d) RF1, (e, f) $TB_{10.8}$, (g, h) TB_{19GHz_H}, and (i, j) TB_{85GHz_H} for two precipitation cases based on the merged datasets.

The distribution of radar reflectivity factor along the AB (as shown in the Fig. 4a) profile in Fig. 5a reveals that stratiform precipitation does not extend vertically beyond 8 km, with some areas exhibiting stratification. A shallow bright band is observed at a height of 4 km. The radar reflectivity factor of the precipitation is generally below 32 dBZ, indicating weak precipitation activity. Figure 5c shows that the reflectivity of the 0.63 μm channel varies mainly between 0.5 and 0.8. The 1.6 μm channel varies between

324   0.1 and 0.3, with these low signal levels further suggesting the presence of numerous ice-phase regions.

325   The change in the brightness temperature profile shows that the top of the stratiform precipitation cloud

326   has a higher temperature and correspondingly lower cloud top height (Fig. 5e). The microwave brightness

327   temperature values vary uniformly between 250 and 270 K, which may be strongly influenced by the

328   surface emissivity and thus may not serve as an accurate indicator (Fig. 5i).

329
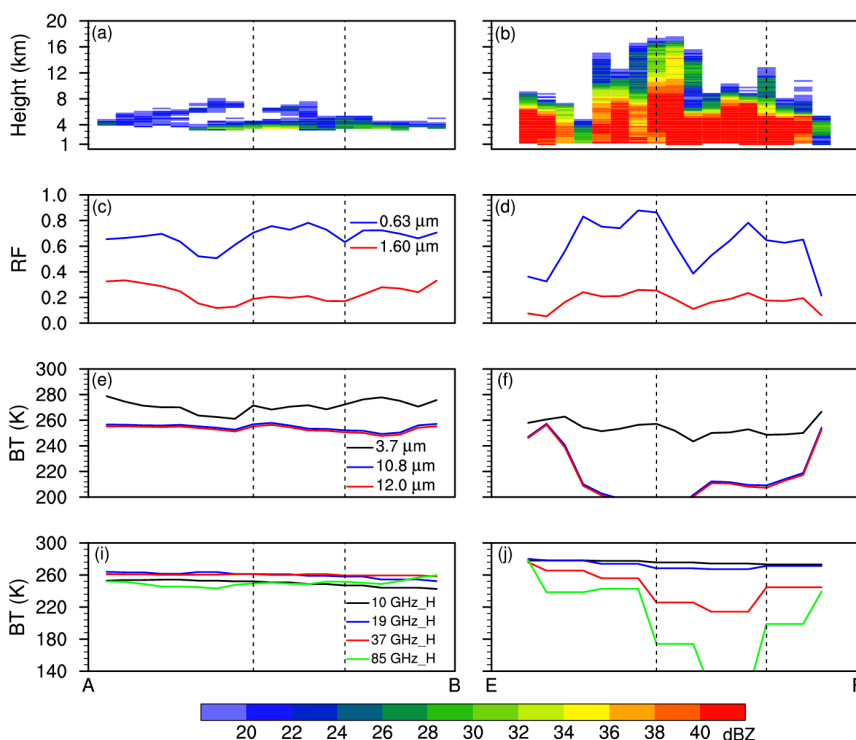
330
331   **Figure 5. The vertical cross sections of (a, b) the radar reflectivity factor, (c, d) reflectivity, (e, f) infrared**
332   **brightness temperatures, (i, j) microwave brightness temperature along the A-B and E-F line as shown in Fig**
333   **4.**

334

335   Figure 5b shows that the radar reflectivity factor presents an uneven distribution in both vertical and

336   horizontal directions due to the irregular movement of precipitation particles in the precipitation cloud

337   with the airflow. The echo top height can reach up to 17 km, which also means that strong convection

338   occurs here. In addition, the radar reflectivity factor of near-surface exceeds 38 dBZ, indicating heavy

339   precipitation near the surface. RF1 varies from 0.3 to 0.9, which means that the COT is unevenly

340   distributed. RF2 does not vary strongly, suggesting that the phase distribution in the cloud is uniform and

341   mostly ice-phase particles (Fig. 5d). The brightness temperature of far-infrared in the region of strong

342 convective development is lower than the other locations (Fig. 5f). Meanwhile, the height of the cloud

343 top is higher in the corresponding region. TB_{10GHz_H} and TB_{19GHz_H} vary uniformly and does not

344 respond well to precipitation. The low value area of the TB_{37GHz_H} and TB_{85GHz_H} tend to correspond

345 well to areas of strong precipitation, as shown by the location of the dotted dashes in Fig. 5j. There are

346 often filled with a high concentration of ice-phase particles in the areas of strong precipitation, leading

347 to strong scattering signal.

348

6 Data availability

350 The rain cell precipitation parameters and visible/infrared and microwave signal datasets used in this

351 paper are accessible at https://doi.org/10.5281/zenodo.8352587.

352

7 Discussion and conclusions

354 We establish a new rain cell precipitation parameter and visible infrared and microwave signal dataset

355 combining with the multi-instrument observation data on TRMM. PR provides the three-dimensional

356 precipitation structure of the rain cell, VIRS provides the spectral signal of the top of the rain cell, and

357 TMI provides the phase information of the particles inside the rain cell. The purpose of this dataset is to

358 promote the three-dimensional study of rain cell precipitation system, and reveal the spatial and temporal

359 variations of the scale morphology and intensity of the system.

360 First, we compare the difference between the MBR rain cell identification method and the BFE rain

361 cell identification method in describing rain cell shape. The two methods are mainly different in the

362 geometric parameters such as L, W, α, S, and β. According to the parameter calculation results, both

363 methods can reflect the geometric characteristics of rain cells effectively. Compared with the MBR

364 method, the BFE method can obtain the fitting result of the smallest rain cell area and its β value is

365 correspondingly larger than that of the MBR method. However, we adopt the MBR method to identify

366 rain cells in the new dataset because it can simplify the data storage volume.

367 Second, we calculate other parameters of two types of rain cell, including vertical geometric

368 parameters (average cloud top height, horizontal scale, spatial morphology, and so on) and physical

369 parameters (average rain rate, maximum reflectivity factor and its corresponding height, average visible

370 reflectivity, average brightness temperature, and so on). The statistical results show that the defined

371   parameters can effectively reflect the three-dimensional morphology of rain cells and the development

372   state of precipitation system, which can provide reference for exploration of the relationship between

373   rain cell morphology parameters and precipitation.

374   Third, we use the new dataset to analyze the distribution of precipitation parameters, cloud top

375   radiation signal, and brightness temperatures and the profile characteristics of two rain cells. The study

376   shows that merged dataset can significantly display the features of the original dataset. For the stratiform

377   rain cell, the rain rate is relatively small, with high cloud top brightness temperature, low cloud top height,

378   and weak vertical movement. For the convective rain cell, the rain rate is large and the distribution is

379   uneven with low cloud top brightness temperature, high cloud top height, and strong vertical movement.

380   The difference of parameter distribution between two types of rain cells is obvious, which lays a

381   foundation for the subsequent study on the characteristics of precipitation.

382   To further explore the characteristics of rain cell, the cloud parameters based on the signal retrieval

383   from the TRMM VIRS data and the latent heat of precipitation inside the rain cell will be added to the

384   dataset. This work is currently in progress but will not be covered in this study due to the limited length

385   of the paper. The dataset will support the research on the development mechanism of precipitation system

386   and promote the progress of precipitation model simulation in the future. With the continuous

387   development of satellite technology, the dataset will add longer time scale data and more effective

388   parameters.

389

390   Author contribution. ZW and YF prepared the data in the standardized format. ZW uploaded the data
391   in the data repository and prepared the manuscript with contribution from YF. All the authors discussed
392   the concepts and edited the manuscript.

393

394   Competing interests. The authors declare that they have no conflict of interest.

395

398

401

402   Review statement.

403

404

405

References

Austin, P. M. and Houze, R. A.: Analysis of the structure of precipitation patterns in New England, J. Appl. Meteorol., 11, 926-935, https://doi.org/10.1175/1520-0450(1972)011<0926:Aotsop>2.0.Co;2, 1972.

Awaka, J.: A three-dimensional rain cell model for the study of interference due to hydrometeor scattering, J. Commun. Res. Lab., 36, 13-44, 1989.

Awaka, J., Iguchi, T., Kumagai, H., and Okamoto, K.: Rain type classification algorithm for TRMM precipitation radar, IEEE International Geoscience and Remote Sensing Symposium Proceedings. Remote Sensing – A Scientific Vision for Sustainable Development, Singapore, 3–8 August 1997, https://doi.org/10.1109/IGARSS.1997.608993, 1997.

Bacchi, B., Ranzi, R., and Borga, M.: Statistical characterization of spatial patterns of rainfall cells in extratropical cyclones, J. Geophys. Res.-Atmos., 101, 26277-26286, https://doi.org/10.1029/96jd01381, 1996.

Begum, S. and Otung, I. E.: Rain cell size distribution inferred from rain gauge and radar data in the UK, Radio. Sci., 44, RS2015, https://doi.org/10.1029/2008RS003984, 2009.

Capsoni, C., Fedi, F., Magistroni, C., Paraboni, A., and Pawlina, A.: Data and theory for a new model of the horizontal structure of rain cells for propagation applications, Radio. Sci., 22, 395-404, https://doi.org/10.1029/RS022i003p00395, 1987.

Chen, Y. L., Zhang, A. Q., Fu, Y. F., Chen, S. M., and Li, W. B.: Morphological characteristics of precipitation areas over the Tibetan Plateau measured by TRMM PR, Adv. Atmos. Sci., 38(4), 677-689, https://doi.org/10.1007/s00376-020-0233-1, 2021.

Durden, S. L., Im, E., Haddad, Z. S., and Li, L.: Comparison of TRMM precipitation radar and airborne radar data, J. Appl. Meteorol., 42, 769-774, https://doi.org/10.1175/1520-0450(2003)042<0769:Cotpra>2.0.Co;2, 2003.

Feral, L., Mesnard, F., Sauvageot, H., Castanets, L., and Lemorton, J.: Rain cells shape and orientation distribution in south-west of France, Phys. Chem. Earth B: Hydrol. Oceans Atmos., 25, 1073-1078, https://doi.org/10.1016/s1464-1909(00)00155-6, 2000.

Fu, Y. F.: Cloud Parameyers retrieved by the bispectral reflectance algorithm and associated applications, J. Meteorol. Res-Prc., 28, 965–982, https://doi.org/10.1007/s13351-014-3292-3, 2014.

Fu, Y. F., Chen, Y., Zhang, X., Wang, Y., Li, R., Liu, Q., Zhong, L., Zhang, Q., and Zhang, A.: Fundamental characteristics of tropical rain cell structures as measured by TRMM PR, J. Meteorol. Res-Prc., 34, 1129-1150, https://doi.org/10.1007/s13351-020-0035-5, 2020.

Fu, Y. F., Liu, D., Wang, Y., Yu, R. C., Xu, Y. P., Cheng, R.: Characteristics of precipitating and non-precipitating clouds in typhoon RANAN as viewed by TRMM combined measurements, Acta Meteorologica Sinica, 65, 316-328, https://doi.org/10.3321/j.issn:0577-6619.2007.03.002, 2007a (in Chinese).

Fu, Y. F. and Liu, G. S.: The variability of tropical precipitation profiles and its impact on microwave brightness temperatures as inferred from TRMM data, J. Appl. Meteorol., 40, 2130-2143, https://doi.org/10.1175/1520-0450(2001)040<2130:Tvotpp>2.0.Co;2, 2001.

Fu, Y. F., Liu, Q., Gao, Y., Hong, X. Y., Zi, Y., Zheng, Y. Y., Li, R., and Heng, Z. W.: A feasible method for merging the TRMM microwave imager and precipitation radar data, J. Quant. Spectrosc. Ra., 122, 155-169, https://doi.org/10.1016/j.jqsrt.2012.08.028, 2013.

Fu, Y. F., Liu, P., Liu, Q., Ma, M., Sun, L., and Wang, Y.: Climatological Characteristics of VIRS

450 Channels for Precipitating Cloud in Summer Over the Tropics and Subtropics, J. Atmos. Environ.
451 Optics, 6, 129–140, https://doi.org/10.3969/j.issn.1673- 6141.2011.02.009, 2011 (in Chinese).

452 Fu, Y. F., Luo, J., Luo, S., Chen, G. C., Wang, M. X., Sun, L. L., Sun, N., and Yang, L.: Rainstorm
453 structure of a supercell cloud occurred in Chongqing in May 2018 measured by GPM DPR and GMI,
454 Torrential Rain and Disasters, 41, 1-14, https://doi.org/10.3969/j.issn.1004-9045.2022.01.001, 2021
455 (in Chinese).

456 Fu, Y. F., Yu, R. C., Cui, C. G., Xu, Y. P., Liu, G. S., Liu, Y., Zheng, Y. Y.: The structure characteristics
457 of precipitating clouds over the east Asia based on TRMM Measurements, Torrential Rain and
458 Disasters, 26, 9-20, https://doi.org/10.3969/j.issn.1004-9045.2007.01.003, 2007b (in Chinese).

459 Goldhirsh, J. and Musiani, B.: Rain cell size statistics derived from radar observations at Wallops
460 Island, Virginia, IEEE Trans. Geosci. Remote Sens., GE-24, 947-954,
461 https://doi.org/10.1109/TGRS.1986.289711, 1986.

462 He, H. Z., Cheng, M. H., and Zhou, F. X.: 3D structure of rain and cloud hydrometeors for Typhoon
463 Kujira (0302), Chinese Journal of Atmospheric Sciences, 30, 491-503, https://doi.org/
464 10.3878/j.issn.1006-9895.2006.03.12, 2006 (in Chinese).

465 Houze, R. A.: Structures of atmospheric precipitation systems: A global survey, Radio. Sci., 16, 671-
466 689, https://doi.org/10.1029/RS016i005p00671, 1981.

467 Houze, R. A.: Stratiform Precipitation in Regions of Convection: A Meteorological Paradox?, B.
468 Am. Meteorol. Soc., 78, 2179–2196, https://doi.org/10.1175/1520-
469 0477(1997)078<2179:SPIROC>2.0.CO;2, 1997.

470 Houze, R. A., Jr., Rasmussen, K. L., Zuluaga, M. D., and Brodzik, S. R.: The variable nature of
471 convection in the tropics and subtropics: A legacy of 16 years of the Tropical Rainfall Measuring
472 Mission satellite, Rev Geophys, 53, 994-1021, https://doi.org/10.1002/2015RG000488, 2015.

473 Konrad, T. G.: Statistical models of summer rainshowers derived from fine-scale radar observations,
474 J. Appl. Meteorol., 17, 171-188, https://doi.org/10.1175/1520-
475 0450(1978)017<0171:SMOSRD>2.0.Co;2, 1978.

476 Kozu, T., Kawanishi, T., Kuroiwa, H., Oikawa, M., Kumagai, H., Okamoto, K., Okumura, M.,
477 Nakatsuka, H., and Nishikawa, K.: Development of precipitation radar onboard the Tropical Rainfall
478 Measuring Mission (TRMM) satellite., IEEE T. Geosci. Remote. Sens., 39, 102-116,
479 https://doi.org/10.1109/36.898669, 2001.

480 Kummerow, C., Barnes, W., Kozu, T., Shiue, J., and Simpson, J.: The Tropical Rainfall Measuring
481 Mission (TRMM) Sensor Package, J. Atmos. Ocean. Tech., 15, 809-817,
482 https://doi.org/10.1175/1520-0426(1998)015<0809:TTRMMT>2.0.Co;2, 1998.

483 Kummerow, C., Simpson, J., Thiele, O., Barnes, W., Chang, A. T. C., Stocker, E., Adler, R. F., Hou,
484 A., Kakar, R., Wentz, F., Ashcroft, P., Kozu, T., Hong, Y., Okamoto, K., Iguchi, T., Kuroiwa, H., Im,
485 E., Haddad, Z., Huffman, G., Ferrier, B., Olson, W. S., Zipser, E., Smith, E. A., Wilheit, T. T., North,
486 G., Krishnamurti, T., and Nakamura, K.: The Status of the Tropical Rainfall Measuring Mission
487 (TRMM) after two years in orbit, J. Appl. Meteorol. Climatol, 39, 1965-1982,
488 https://doi.org/10.1175/1520-0450(2001)040<1965:Tsottr>2.0.Co;2, 2000.

489 Lau, K. M. and Wu, H. T.: Characteristics of Precipitation, Cloud, and Latent Heating Associated
490 with the Madden-Julian Oscillation, J. Climate, 23, 504–518,
491 https://doi.org/10.1175/2009jcli2920.1, 2010.

492 Li, R. and Fu, Y. F.: Tropical precipitation estimated by GPCP and TRMM PR observations, Adv.
493 Atmos. Sci., 22, 852-864, https://doi.org/10.1007/BF02918685, 2005.

494 Liu, C. T. and Zipser, E.: Regional variation of morphology of organized convection in the tropics
495 and subtropics, J. Geophys. Res. Atmos., 118, 453-466, https://doi.org/10.1029/2012JD018409,
496 2013.

497 Liu, C. T., Zipser, E. J., Cecil, D. J., Nesbitt, S. W., and Sherwood, S.: A cloud and precipitation
498 feature database from nine years of TRMM observations, J. Appl. Meteorol. Climatol., 47, 2712-
499 2728, https://doi.org/10.1175/2008jamc1890.1, 2008.

500 Liu, C. T. and Zipser, E. J.: "Warm Rain" in the tropics: Seasonal and regional distributions based
501 on 9 yr of TRMM data, J. Climate, 22, 767-779, https://doi.org/10.1175/2008jcli2641.1, 2009.

502 Liu, G. S. and Fu, Y. F.: The characteristics of tropical precipitation profiles as inferred from satellite
503 radar measurements, J. Meteor. Soc. Japan, 79, 131-143, https://doi.org/10.2151/jmsj.79.131, 2001.

504 Liu, Q. and Fu, Y. F.: Comparison of radiative signals between precipitating and non-precipitating
505 clouds in frontal and typhoon domains over East Asia, Atmos. Res., 96, 436–446,
506 https://doi.org/10.1016/j.atmosres.2010.02.003, 2010.

507 Luo, S., Fu, Y. F., Zhou, S. N., Wang, X. F., and Wang, D. Y.: Analysis of the relationship between
508 the cloud water path and precipitation intensity of mature typhoons in the northwest Pacific ocean,
509 Adv. Atmos. Sci, 37, 359-376, https://doi.org/10.1007/s00376-020-9204-9, 2020.

510 Nesbitt, S. W., Zipser, E. J., and Cecil, D. J.: A census of precipitation features in the tropics using
511 TRMM: Radar, ice scattering, and lightning observations, J. Climate, 13, 4087-4106,
512 https://doi.org/10.1175/1520-0442(2000)013<4087:ACOPFI>2.0.Co;2, 2000.

513 Nesbitt, S. W., Zipser, E. J., and Cecil, D. J.: A census of precipitation features in the tropics using
514 TRMM Radar, ice scattering, and lightning observations, J. Climate, 13, 4087-4106,
515 https://doi.org/10.1175/1520- 0442(2000)013<4087:ACOPFI>2.0.CO;2, 1999.

516 Oki, T. and Kanae, S.: Global hydrological cycles and world water resources, Science, 313, 1068–
517 1072, https://doi.org/10.1126/science.1128845, 2006.

518 Petty, G.W.: Physical retrievals of over-ocean rain rate from multichannel microwave imagery. Part
519 I: Theoretical characteristics of normalized polarization and scattering indices, Meteorl. Atmos.
520 Phys., 54, 79–99, https://doi.org/10.1007/BF01030053, 1994a.

521 Petty, G.W.: Physical retrievals of over-ocean rain rate from multichannel microwave imagery. Part
522 II: Algorithm implementation, Meteorl. Atmos. Phys., 54, 101–121,
523 https://doi.org/10.1007/BF01030054, 1994b.

524 Rutledge, S. A., Cifelli, R., and Nesbitt, S. W.: Storm morphology and rainfall characteristics of
525 TRMM precipitation features, Mon. Weather Rev., 134, 2702-2721,
526 https://doi.org/10.1175/mwr3200.1, 2006.

527 Sauvageot, H., Mesnard, F., and Tenório, R. S.: The relation between the area-average rain rate and
528 the rain cell size distribution parameters, J. Atmos. Sci., 56, 57-70, https://doi.org/10.1175/1520-
529 0469(1999)056<0057:TRBTAA>2.0.Co;2, 1999.

530 Schumacher, C. and Houze, R. A.: The TRMM precipitation radar's view of shallow, isolated rain,
531 J. Appl. Meteorol., 42, 1519-1524, https://doi.org/10.1175/1520-
532 0450(2003)042<1519:TTPRVO>2.0.CO;2, 2003.

533 Simpson, J., Kummerow, C., Tao, W.-K., and Adler, R. F.: On the Tropical Rainfall Measuring
534 Mission (TRMM), Meteorol. Atmos. Phys., 60, 19-36, https://doi.org/10.1007/BF01029783,1996.

535 Sun, L. L. and Fu, Y. F.: A new merged dataset for analyzing clouds, precipitation and atmospheric
536 parameters based on ERA5 reanalysis data and the measurements of the Tropical Rainfall Measuring
537 Mission (TRMM) precipitation radar and visible and infrared scanner, Earth Syst. Sci. Data, 13,

538   2293-2306, https://doi.org/10.5194/essd-13-2293-2021, 2021.

539   Viltard, N., Kummerow, C., Olson, W. S., and Hong, Y.: Combined use of the radar and radiometer

540   of TRMM to estimate the influence of drop size distribution on rain retrievals, J. Appl. Meteorol.,

541   39, 2103-2114, https://doi.org/10.1175/1520-0450(2001)040<2103:Cuotra>2.0.Co;2, 2000.

542   Wu, Z. H. and Fu, Y. F.: A new dataset of rain cell generated from observations of the Tropical

543   Rainfall Measuring Mission (TRMM) precipitation radar and visible and infrared scanner and

544   microwave imager [dataset], Zenodo, https://doi.org/10.5281/zenodo.8352587, 2023.

545   Yuter, S. E. and Houze, R. A.: Three-Dimensional kinematic and microphysical evolution of florida

546   cumulonimbus. Part II: frequency distributions of vertical velocity, reflectivity, and differential

547   reflectivity, Mon. Weather Review., 123, 1941-1963, https://doi.org/10.1175/1520-

548   0493(1995)123<1941:Tdkame>2.0.Co;2, 1995.

549   Zhang, A. Q., Chen, C., Chen, Y. L., Li, W. B. A., Chen, S. M., and Fu, Y. F.: Resilient dataset of

550   rain clusters with life cycle evolution during April to June 2016-2020 over eastern Asia based on

551   observations from the GPM DPR and Himawari-8 AHI, Earth Syst. Sci. Data, 14, 1433-1445,

552   https://doi.org/10.5194/essd-14-1433-2022, 2022.

553   Zipser, E. J. and Lutz, K. R.: The vertical profile of radar reflectivity of convective cells: A strong

554   indicator of storm intensity and lightning probability?, Mon. Weather Rev., 122, 1751-1759,

555   https://doi.org/10.1175/1520-0493(1994)122<1751:Tvporr>2.0.Co;2, 1994.